Plasmonic Nanogap Tilings: Light-Concentrating Surfaces for Low-Loss Photonic Integration

Paul M. Z. Davies, Joachim M. Hamm, Yannick Sonnefraud, Stefan A. Maier, and Ortwin Hess*

The Blackett Laboratory, Department of Physics, Imperial College London, South Kensington Campus, London SW7 2AZ, U.K.

ABSTRACT Owing to their ability to concentrate light on nanometer scales, plasmonic surface structures are ideally suited for on-chip functionalization with nonlinear or gain materials. However, achieving a high effective quantum yield across a surface requires not only strong light localization but also control over losses. Here, we report on a particular class of tunable low-loss metasurfaces featuring dense arrangements of nanometer-sized focal points on a photonic chip with an underlying waveguide channel. Guided within the plane, the photonic wave evanescently couples to the nanogaps, concentrating light in a lattice of hot-spots. In studying the energy transfer between photonic and plasmonic channels of single trimer molecules and triangular nanogap tilings in dependence on element size, we identify different regimes of operation. We show that the product of field enhancement, propagation length, and element size is close to constant in both the radiative and subwavelength regimes, opening pathways for device designs that combine high-field enhancements with large propagation lengths.

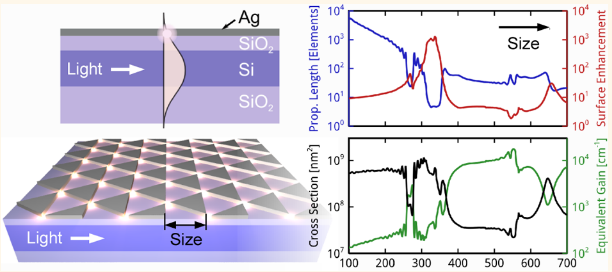

KEYWORDS: nanogap tiling · low-loss plasmonics · silicon photonics · waveguide integration · mode hybridization

Mediated by subwavelength interactions with metallic particles, nanoplasmonic surfaces can alter the localization and propagation characteristics of light at interfaces.[1-3] The steady progress in lithographic[4,5] and self-assembly techniques[6,7] makes it possible to shape metallic surface elements with increasing precision, reaching toward sub-nanometer scales.[8] In the wake of this technological development, schemes involving coupled plasmonic particle clusters and arrays have been designed, fabricated, and studied, exploring their potential to slow or stop light,[9-11] to nanofocus light in the gaps between or at the edges of the nanoparticles,[12,13] to resonantly transport energy along particle chains,[14] to control the phase[15-17] and polarization,[16,18] and to refract light at negative angles.[15,17]

As research continues to explore nanoplasmonic surfaces with engineered optical properties and their functionalization with nonlinear and quantum gain[19,20] materials as diverse as gases,[21] semiconductors,[22] dyes,[23] and graphene,[24] there is a growing gap between the wealth of potential applications and practical concepts for on-chip integration with photonic technologies. In fact, until now, plasmonic and metamaterial surfaces are mostly operated out-of-plane, *i.e.*, by illumination under normal incidence or evanescent excitation with near-field microscope tips,[25-27] two well-established techniques that are convenient to perform, yet with limited potential for on-chip integration. Fundamentally, integration with photonic circuitry requires keeping light confined and in interaction with the structured surface, without inducing uncontrolled scattering or excessive dissipative loss. The usual trade-off is that a stronger confinement of light to the metallic surface increases attenuation and heat generation due to Ohmic losses.[28-30] Hybrid metal–dielectric waveguide structures[31-34] offer one possibility to break the interdependency of loss and localization, but require careful design to achieve good loss performance and compatibility with established photonic architectures. Furthermore, from a fabrication and integration perspective, it is highly desirable to establish a platform where light waves, guided within a photonic layer, can be manipulated on subwavelength scales

* Address correspondence to o.hess@imperial.ac.uk.

Received for review May 14, 2013 and accepted July 4, 2013.

10.1021/nn402432m

using metallic nanostructures on the surface.[35] Such hybrid platforms may not only provide well-defined interfaces for on-chip integration of plasmonic devices (*e.g.*, sensors or spectroscopic elements) with photonic signal-processing circuits but also offer practical routes toward active nanoplasmonic components that exploit the enhanced surface interaction with fluorescent,[36] magneto-optic,[37] or nonlinear materials.[21]

In this article we report on a particular class of integrated plasmonic surface structures, plasmonic nanogap tilings (NGTs), featuring dense lattices of focal points (Figure 1). To understand the general properties of plasmonic NGTs, we theoretically study one of the simplest structures: triangular surface patches of fixed orientation arranged in a triangular lattice. The chosen combination of shape and lattice was guided by our aim to concentrate light in a dense array of hot-spots to achieve a strong enhancement of the surface fields.

The surface structure is fully characterized by the pitch $L = a\sqrt{3}/2$, given by the projection of lattice vectors $\vec{a}_1$ and $\vec{a}_2$ in the propagation direction, the gap G, and the element corner rounding of diameter D (Figure 1a). The triangular NGTs borrow symmetry and light-enhancing properties from the trimer molecule. As shown in Figure 1a, both the C_{3v} symmetry of the molecule and two sets of directional axes of excitation ($+z$ and $-z$) are retained in the assembled 2D tiling (Figure 1c).

We consider 30 nm thick silver (Ag) structures on top of a planar dielectric stack consisting of a silicon oxide (SiO_2) substrate, a planar w = 220 nm thick silicon (Si) waveguide, and a SiO_2 buffer layer of tunable thickness b (Figure 1b). To maintain the lateral mode profile, we operate at a fixed wavelength of λ_0 = 1550 nm where the guiding Si layer supports only the fundamental transverse electric (TE) and magnetic (TM) modes. At this wavelength, the complex permittivity of the silver[38] can be approximated by $\varepsilon_{Ag} = -127 - 3.38i$.

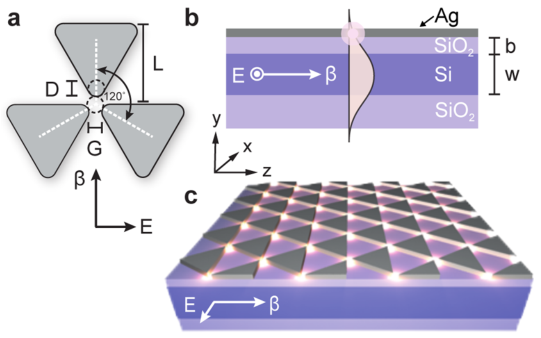

Figure 1. Triangular nanogap tiling made of C_{3v} symmetric trimer molecules (a) that are densely arranged on the top of a dielectric stack (b). The TE-polarized photonic field propagates with $\beta = n_{eff}k_0$ inside the silicon waveguide (w) while being evanescently focused into bright spots on the surface (c). Both the corner diameter of the elements and the gaps are set to scale with the pitch L (*i.e.*, $G = D = L/10$).

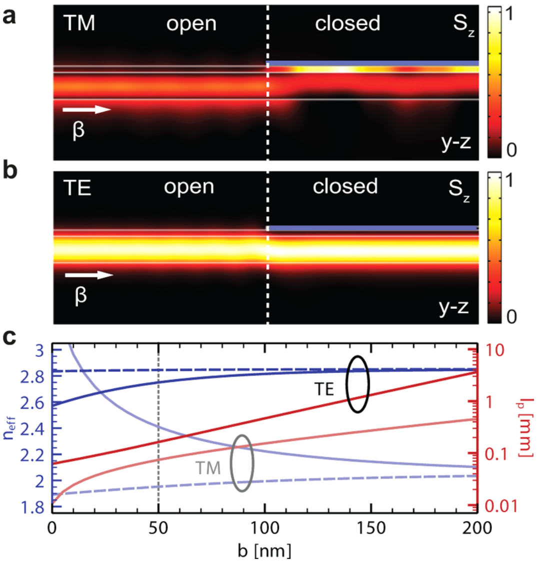

Figure 2. (a and b) z-Component of the Poynting vector for TM (a) and TE (b) mode scattering at the edge of a 30 nm thick silver layer separated by a SiO_2 buffer of height b = 50 nm from the Si waveguide. (c) In directly exciting a plasmonic mode in the buffer, the TM mode experiences a strong mismatch of effective indices (light blue lines) and a consistently lower propagation length (light red lines) than the TE mode (dark lines) for equivalent buffer sizes b. Dashed lines correspond to the open; solid lines, to the closed waveguide sections.

RESULTS AND DISCUSSION

Waveguide Integration. To characterize the fundamental properties of the hybrid platform, we first study modes impinging on the interface between the open (*i.e.*, uncovered) and closed (*i.e.*, metal covered) waveguide sections. For TM polarization (Figure 2a), the mode hybridizes[33] with the surface plasmon polariton (SPP) mode at the metal–buffer interface, concentrating the energy in the low-index buffer.[39–41] As a consequence, both the mode profiles and the effective refractive index (Figure 2c; light blue lines) between the two sections mismatch strongly, in particular for b < 10 nm. In contrast, the TE mode (Figure 2b) retains its photonic character across the discontinuity and, while being slightly pushed down into the low-index substrate, experiences a considerably smaller perturbation of its profile and a change in its effective index (Figure 2c; dark blue lines). More specifically, at b = 50 nm, the effective refractive index mismatch, Δn_{eff}, between the open and closed sections for a TE excitation amounts to −0.1, compared to +0.45 in the TM case. We also note that the propagation length l_p^{TE} of the TE mode is consistently larger than that of the TM mode and rises strictly exponentially with increasing buffer height (Figure 2c; red lines, right axis). This exponential behavior at small buffer heights indicates that, for TE excitation, losses are induced by the evanescent tail of the mode profile touching the metallic surface rather than the direct coupling as in the case of the TM mode. At b = 50 nm, we record a value of

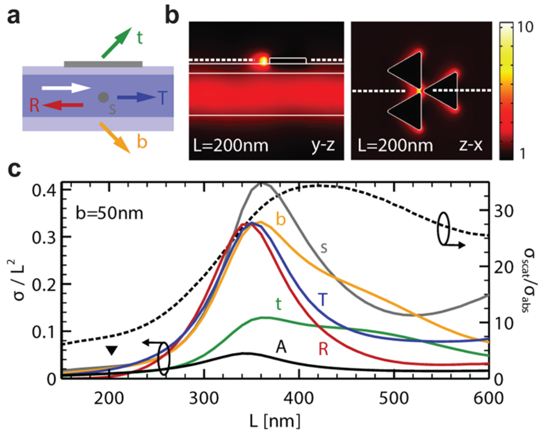

Figure 3. (a) Schematic of the backward (R; red), forward (T; blue), top (t; green), bottom (b; orange), and sideways (s; gray line) scattering channels of a single trimer antenna. (b) Electric field amplitude in $y-z$ plane and $z-x$ plane at positions indicated by the dashed white lines for an isolated trimer nanoantenna of dimension $L = 200$ nm. (c) Scattering cross sections for the various scattering channels (left axis), absorption cross-section (black line, left axis), and ratio between scattering/absorption cross sections (dashed line, right axis).

$l_p^{TE} \approx 134\ \mu$m, roughly twice as high as the corresponding TM value, confirming that the TE mode not only features the better matched mode profile but is also more favorable in terms of dissipative loss.

Trimer Surface Antenna: Scattering Spectra. Field concentration in the focal points is achieved *via* evanescent interaction of the guided TE mode with surface elements. To explore this mechanism, we first consider an isolated trimer molecule[42] (Figure 1a) of individual element size L. The isolated trimer can be understood as a plasmonic surface antenna that is evanescently driven by the photonic field, absorbing and scattering energy into the various in- and out-of-plane channels (Figure 3a). Figure 3c shows the scattering and absorption cross sections associated with the different channels. The ratio of scattered energy to the absorbed energy (dashed line, right axis) shows that the absorption is 5−35 times lower than scattering, as the antenna cannot be considered small compared to the effective wavelength of $\lambda_{\mathrm{eff}} \approx 544$ nm. For $L < 200$ nm, in the subwavelength regime, the scattering cross sections are smaller than $0.04L^2$. With increasing L, the various scattering cross sections (left axis) rise and peak at $L \approx 350$ nm, due to the excitation of localized surface plasmon resonances (LSPRs). Owing to the strong refractive index mismatch between the air cladding and silicon waveguide, the top scattering is weakest while the scattering to the side achieves the highest cross-section of just above $0.4L^2$. Beyond the dipolar resonance $L > 400$ nm the scattering cross sections drop, except those related to the out-of-plane scattering (channels t and b) that exhibit a characteristic shoulder. This suggests the presence of another radiative resonance at around $L = 500$ nm. The exceptional stability of the driving photonic field, even at resonance, is one of the characteristics of TE excitation that makes this configuration inherently suitable for the optically driven chip-integrated plasmonic antennas.

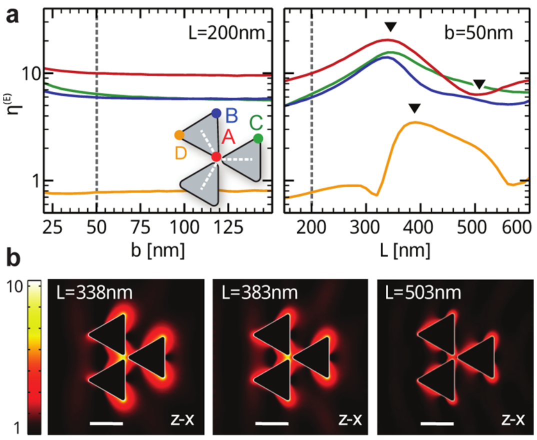

Figure 4. (a) Surface field enhancement $\eta^{(E)}$ at the four corner points A (red), B (blue), C (green), and D (orange) in dependence on buffer height b (for fixed $L = 200$ nm) and size L (for fixed buffer height $b = 50$ nm). (b) Color plots of $\log(\eta^{(E)})$ in the $z-x$ plane for $L = 338$ nm, $L = 338$ nm, and $L = 503$ nm show the distribution of intensities.

Trimer Surface Antenna: Field Enhancement. Despite the weaker evanescent surface interaction, the TE-polarized photonic field can lead to strong lateral charge separation within the metallic surface elements. This can lead to capacitive coupling in the nanogaps between the elements, inducing strong fields that peak at resonance.[43,44] As shown in Figure 3b, the field concentrates on the surface into bright spots at the corners of the antenna, while the propagating field in the waveguide below remains mostly unperturbed.

To quantify the achieved light concentration, we measure the relative surface enhancement, $\eta^{(E)}$, of the electric field at the different corners of the trimer (Figure 4a; inset) by dividing the field amplitude averaged over a small volume around the respective corner by the same surface field without the antenna, *i.e.*, $\eta_\circ^{(E)} = |E(\mathbf{r}_\circ)|/|E_0|$ ($\circ = A, B, C, D$). The results in Figure 4 give a strong indication that the spot enhancements are largely independent of buffer height (Figure 4a; left panel), as the evanescent surface field is effectively funneled into the central focus point A without a significant perturbation of the mode propagating within the waveguide. With increasing size L, the antenna (Figure 4a; right panel) becomes resonant (at $L \approx 338$ nm) and the field enhancement at the center position increases from $\eta_A^{(E)} \approx 10$ to $\eta_A^{(E)} \approx 20$. The position of the enhancement peaks (and dips) depends critically on the position of evaluation. The most distinct features are the peaks of $\eta_A^{(E)}$, $\eta_B^{(E)}$, and $\eta_C^{(E)}$ at around $L \approx 338$ nm, the broad peak of $\eta_D^{(E)}$ at $L \approx 383$ nm, and the dip of $\eta_A^{(E)}$ at around $L \approx 503$ nm (see markers in Figure 4a). Figure 4b shows the two resonant states of the antenna, characterized by a strong lateral charge

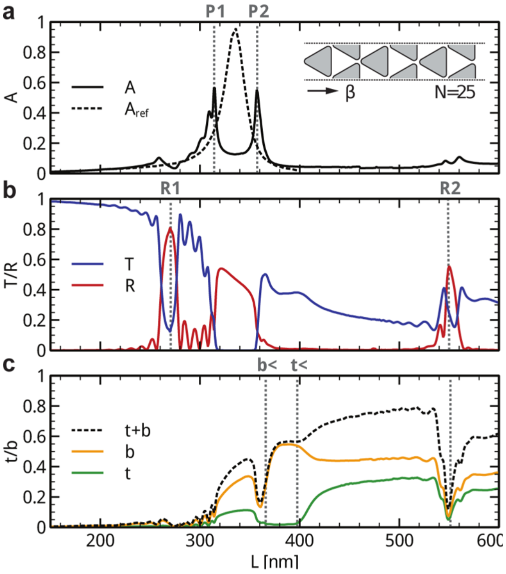

Figure 5. Absorption and scattering coefficients of the triangular NGT recorded over pitch length *L*. (a) Absorption coefficient *A* of the NGT for in-plane (solid) and out-of-plane (dashed) excitation; (b) in-plane transmission *T* (blue) and reflection *R* (red) coefficients; and (c) coefficients for out-of-plane scattering into the SiO_2 substrate *b* (yellow) and air superstrate *t* (green) and the sum $t + b$ (dashed). The colors of the lines match those of Figure 3a.

separation ($L \approx 338$ nm; left panel) and an additional longitudinal charge separation ($L \approx 383$ nm; middle panel). With increasing size *L*, additional nodal planes in the longitudinal direction become visible ($L \approx 503$ nm; right panel) as a signature of wave retardation. As the element size becomes comparable to the effective wavelength of the waveguide mode, the polarizing electric field changes orientation across the antenna, exciting higher order (subradiant) modes. This retardation effect also illuminates the otherwise dark corner *D* and causes, in weakening the lateral resonance, a decrease of the enhancement in the center.

Nanogap Tiling: Scattering Spectra. Having established how light is focused and scattered by a single trimer molecule on the surface, we proceed to study the optical characteristics of the triangular nanogap tiling, which can be understood as a dense array of coupled trimer molecules. These structures are of particular practical interest, as they allow for in-plane excitation of a dense array of bright spots accessible from the surface. For the following we chose a laterally periodic array of $N = 25$ triangular elements in the propagation direction. To gain an understanding of the photonic and plasmonic resonances of integrated NGTs, we first compare the change of absorption of the triangular NGTs for out-of-plane excitation (*via* total internal reflection) and in-plane excitation (from the waveguide) with varying element pitch *L*.

Figure 5a (solid black line) shows the calculated absorption spectrum for in-plane excitation for buffer and waveguide heights of $b = 50$ nm and $w = 220$ nm, respectively. The absorption spectrum shows two distinct peaks, marking, as can be seen from the spectra in Figure 5b, the edges of a transmission stop-band. To understand the origin of the hybridization in the waveguide-integrated configuration, we compare the in-plane absorption spectrum with the absorption of the NGT under out-of-plane excitation. We place the NGT on a thick buffer of SiO_2, thereby isolating the NGT from the influence of the silicon layer. To recreate the same conditions of excitation as for in-plane excitation, we inject a plane wave from a semi-infinite Si substrate (prism) below the buffer at an incident angle of $\theta_{inc} = \arcsin(n_{eff}/n_{Si})$. At this angle, the injected plane wave experiences total internal reflection at the Si/SiO_2 interface and can evanescently couple to the surface tiling only with an in-plane projection of the wave vector that precisely matches the propagation constant $\beta = n_{eff}k_0$ of the waveguide mode. The result, plotted as a dashed line in Figure 5a, shows a single broad plasmonic resonance at around $L \approx 340$ nm centered between the two in-plane absorption peaks. The splitting of the plasmonic resonance and the emergence of a transmission stop-band is a result of the interaction between the plasmonic resonances of the tiling with the propagating mode in the waveguide. When the trimer molecules are coupled in a dense array, the LSPRs couple to a plasmonic band that supports propagation of SPPs along the chain of nanoparticles.[14] The mutual coupling of the propagating plasmonic and photonic modes leads to the formation of waveguide–plasmon polaritons, which, due to the strong coupling (low buffer height), anticross at the point where the frequencies and *k*-vectors of the plasmonic and waveguide modes match.[45] As a consequence of the mode hybridization, the observed mode splitting increases with decreasing buffer size as the coupling parameter between the waveguide and the surface plasmonic modes becomes exponentially stronger.

A fundamental difference between in-plane and out-of-plane excitation concerns the number of available scattering channels. While plane-wave ATR spectroscopy measurements record energy transfer into absorption (A), transmission (T), and reflection (R) channels, one must, for integrated designs, also consider the scattering into the superstrate (t; top) and the substrate (b; bottom). In Figure 5b/c we show the scattering coefficients of the triangular NGT over *L* in the range 200 to 650 nm. With the structure becoming resonant to the effective wavelength ($L \gtrsim \lambda_{eff}/2$), it acts as a plasmonic crystal.[46−48] Both plasmonic and photonic scattering are mediated by the triangular lattice of the NGT. In the propagation direction, the projections of the incident wave vector (the propagation constant β) on the reciprocal lattice vectors ($\vec{a}_1$ and $\vec{a}_2$) are equal. The *k*-matching condition $k_s = \beta \pm m2\pi/L$ dictates that the in-plane projection of the scattered wave vector equals the incident wave vector β plus multiples m of the effective lattice vector $2\pi/L$. Using $k_s = n_s k_0 \sin(\theta_s)$ we associate k_s with the scattering angle θ_s relative to the surface-normal and the refractive index n_s of the scattering channel. Resolving this condition with respect to L gives

$$L = \pm m \frac{\lambda_0}{n_{\mathrm{eff}} - n_s \sin(\theta_s)} \quad (1)$$

Apart from the plasmonic stop-band between L_{P1} and L_{P2} (Figure 5a), there are two more stop-gaps (at L_{R1} and L_{R2}) in the spectrum (see Figure 5b), which can be explained by resonant backscattering. Setting $\theta_s = -\pi/2$ and $n_s = n_{\mathrm{eff}}$ in eq 1 gives $L = m\lambda_0/(2n_{\mathrm{eff}})$, the Bragg conditions for the first- and second-order ($m = 1, 2$) reflection peaks at $L_{R1} \approx 280$ nm and $L_{R2} \approx 559$ nm, which are in excellent agreement with Figure 5b. In contrast, out-of-plane scattering into the SiO_2 substrate ($n_s = 1.44$) and air ($n_s = 1.0$) can occur over the whole lower and upper half-space. Again using eq 1, we mark the points for $\theta_s = -\pi/2$ as $L_{t<}$ and $L_{b<}$ for scattering to the top and bottom, respectively. We also note that the second Bragg peak at $L_{R2} \approx 559$ nm always coincides with normal-to-plane scattering into the substrate and superstrate, reducing the proportion of energy transmitted into these channels.

Nanogap Tiling: Surface Field Enhancement. Changing the pitch L of the NGT not only affects the scattering of energy into the various channels but has a strong impact on the concentration of energy on the surface as the plasmonic resonance and localization of fields in the waveguide change. To investigate the enhancement of fields, we (as before) inject a waveguide mode into an NGT with $N = 25$ elements and record the laterally (along x-direction) averaged intensities on the surface $|E_s(z)|^2 = |E(y_s,z)|^2$ and in the center of the waveguide $|E_{wg}(z)|^2 = |E(y_{wg},z)|^2$. To obtain the relative field intensities on the surface and inside the waveguide, we divide by $|E_s^{(0)}|^2 = |E^{(0)}(y_s)|^2$ and $|E_{wg}^{(0)}|^2 = |E^{(0)}(y_{wg})|^2$, the bare intensities without the NGT on the surface (Figure 6; left panels). Finally, to quantify the net enhancement of the field, we average the normalized intensities on the surface and inside the waveguide along the propagation direction (Figure 6; right panels). The results show that the normalized surface intensities peak at the hybrid resonances at L_{P1} and L_{P2}. Both the plasmonic stop-gap and the Bragg resonances inhibit propagation in the waveguide, leading to strong attenuation of the fields in the propagation direction. However, owing to the excitation of SPPs, energy keeps propagating in the form of SPPs on the surface with less attenuation, leading to an elevated surface field enhancement in these spectral regimes (compare Figure 6a and b).

For pitch lengths above the plasmonic resonances, the surface intensities weaken due to the onset of out-of-plane scattering. In contrast, below the first Bragg resonance, in the subwavelength regime, the strength of the surface intensities settles at an average value of ~10, while the average intensity in the waveguide remains ~1 across the length of the NGT. This off-resonant enhancement of surface intensities can be attributed to the lightning rod effect,[49] which leads to a concentration of field strength into the focal points of the NGT without inducing high plasmonic losses.

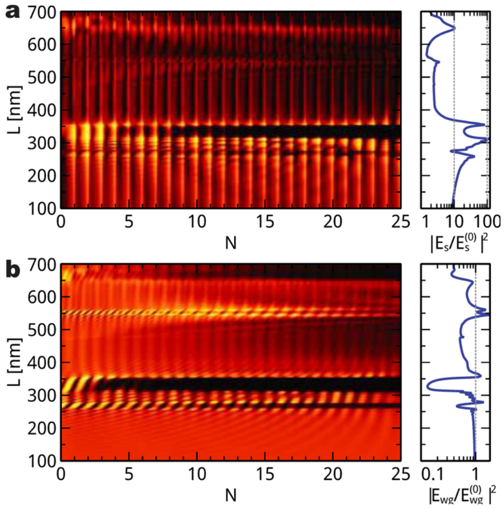

Figure 6. Log plots of the laterally (along x-direction) averaged field intensities (a) at the surface ($y = y_s$) and (b) in the center of the waveguide ($y = y_{wg}$) for an NGT structure with $N = 25$ elements. The corresponding longitudinally averaged intensities are plotted on the right-hand panels.

For functionalization of the surface (*e.g.*, with polymers, dyes, *etc.*) we are interested in the effective enhancements of the linear and nonlinear susceptibilities of the material deposited. To find the enhancement for a particular process, we divide the nth power of the normalized surface field by the normalized electric field within the waveguide and integrate over the area of the NGT. For example the effective intensity enhancement ($n = 2$) is given by

$$\eta_{\mathrm{eff}}^{(I)} = \frac{1}{A}\int_A \frac{|E(x, y_s, z)|^2}{|E(x, y_{wg}, z)|^2}\, dx\, dz \quad (2)$$

The fact that we divide the surface intensities at every point by the intensity in the waveguide underneath allows us to eliminate propagation effects such as attenuation, back-reflection, and standing wave patterns. This approach is valid as the evanescent interaction of the waveguide fields with the surface structure does not involve significant retardation effects. The so-obtained effective enhancement of the surface intensity is plotted in Figure 7a (red line) together with the unitless effective propagation length l_p/L (blue line) over the pitch L. One notices that, in the off-resonant regime, the per element propagation length decreases exponentially for decreasing pitch values, while the effective enhancement of the surface intensity asymptotically approaches a value of ~10. When the

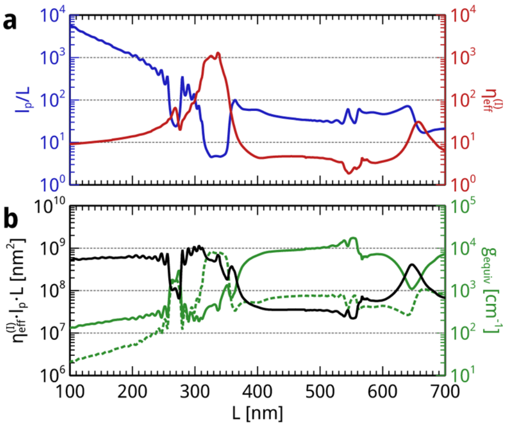

Figure 7. (a) Propagation length of the TE mode in the waveguide (blue line) relative to the element pitch and the effective surface intensity enhancement (red line). (b) Effective attenuation cross-section $\sigma_{eff} = \eta^{(l)}_{eff} l_p L$ (black line) and the equivalent gain coefficients (green lines) required for full loss-compensation. The results for gain on the surface (solid green line) and in the waveguide (dashed green line) differ due to the impact of the confinement factor and field enhancement.

pitch approaches the plasmonic resonance of the NGT at around $L \approx 340$ nm, the effective propagation length is at a minimum as the plasmonic stop-gap prevents propagation of the wave. The effective intensity enhancement is strongest in this regime as the NGT is excited resonantly, leading to high-field concentrations (relative to the waveguide fields) in the gaps that propagate in the form of SPPs along the surface. For pitch values larger than $L \approx 400$ nm, where out-of-plane scattering dominates, the values of $\eta^{(l)}_{eff}$ and l_p/L change only slightly with the pitch.

Nanogap Tiling: Equivalent Gain. Although the achieved intensity enhancement in the subwavelength regime is comparably low, the propagating photonic field experiences low attenuation and remains in interaction with the NGT. To quantify the trade-off between field concentration and attenuation, we introduce an effective attenuation cross-section:

$$\sigma_{eff} = \eta^{(l)}_{eff} l_p L \tag{3}$$

which is shown in Figure 7b (black line). Strikingly, this cross-section is close to constant in the subwavelength regime (below $L = 250$ nm) and in the radiative regime before the second Bragg resonance ($L = 400-550$ nm). In these regimes

$$\eta^{(l)}_{eff} = \frac{\text{const}}{L^2}\left(\frac{l_p}{L}\right)^{-1} \tag{4}$$

which means that the ability of the NGT to concentrate energy on the surface is proportional to the density of hot-spots ($\sim 1/L^2$) and the normalized attenuation (L/l_p). This relation is of particular relevance in the context of device functionalization with nonlinear[50] and gain materials.[51−53] As an application, we imagine an active material deposited on the surface. To fully compensate the dissipative and radiative losses, we require an equivalent gain of

$$g_{equiv} = \frac{1}{\Gamma \eta^{(l)}_{eff} l_p} \tag{5}$$

introducing the confinement factor

$$\Gamma = \frac{\int_{-\infty}^{+\infty} dy \Theta(y) |E^{(0)}(y)|^2}{\int_{-\infty}^{+\infty} dy |E^{(0)}(y)|^2} \tag{6}$$

which quantifies the proportion of energy that interacts with the gain region ($\Theta(y) = 1$ in the gain-filled section and 0 elsewhere). For the given structure we find that $\Gamma \approx 0.0143$ for a layer of 30 nm gain medium deposited on the buffer in between the elements of the plasmonic NGT. The retrieved equivalent gain values are plotted as a green line in Figure 7b. In the subwavelength regime, where the attenuation cross-section reaches a value of $\sim(4-5) \times 10^8$ nm^2, there is a linear increase of the equivalent gain with L from $g_{equiv} \approx 150$ cm^{-1} at $L = 100$ nm to $g_{equiv} \approx 300$ cm^{-1} at $L = 250$ nm. At the first Bragg resonance ($L \approx 270$ nm), the gain values peak at $g_{equiv} \approx 2000$ cm^{-1} before they drop again to values of only $g_{equiv} \approx 200$ cm^{-1} in the plasmonic stop-gap, where the propagation constant is lowest but the effective enhancement highest (see Figure 7a). Beyond the plasmonic resonances, radiative loss dominates and the field enhancement is low. This leads to high equivalent gain values of $\sim 10^4$ cm^{-1} that would be required to compensate attenuation losses. The results illustrate that loss-compensation in the proposed hybrid structure is a realistic prospect even in the resonant plasmonic regime. Finally, we note that using epitaxially grown InGaAsP-based semiconductor structures, gain can also be introduced directly into the waveguide structure. In this case (keeping the geometric dimensions), the confinement factor is $\Gamma \approx 0.82$, but there is no plasmonic field enhancement, resulting in the dashed green line in Figure 7b. While the required gain for loss-compensation is generally lower, this is particularly not true in the regime where the waveguide mode couples to the surface plasmon resonances of the surface.

CONCLUSION

In conclusion, we reported on a new class of low-loss integrated surface structures, plasmonic nanogap tilings (NGTs), which can concentrate light on the surface of a photonic chip in a dense lattice of bright spots. To understand their unique properties, we investigated triangular trimers in an integrated configuration, showing their potential to scatter and concentrate light on the surface of the chip in dependence of their size. For the assembled NGT, we identified different regimes of operation depending on the pitch length: the off-resonant regime, where the NGT acts as true light-concentrating metasurface, and regimes dominated by in-plane (back) scattering, excitation of plasmonic modes, and out-coupling of radiation. Using a novel technique for the extraction of the field enhancement, we were able to define an effective attenuation cross-section, which plateaus in the off-resonant and radiative regimes. The equivalent gain required for loss-compensation on the surface and in the waveguide illustrates that loss-compensation in these structures is realistically possible. The triangular structure that forms the basis of this work is one of many possibilities to cover a surface with a regular 2D tiling. The chosen combination of particle shape (triangles) and crystal lattice (hexagonal) was guided by our aim to concentrate light in a dense array of hot-spots on the surface. Tilings with higher symmetry, such as a checkerboard tiling (diamonds on a square lattice), are possible but do not achieve the same surface field enhancement, as, for a given propagation direction, only half of the nanogaps are excited. We note that waveguide-integrated plasmonic surface arrays are not limited to the passive SOI platform, but can also be integrated on active semiconductor material systems (*e.g.*, III–V semiconductors). While surface functionalization with gain materials was considered in this work, other nonlinear materials can be conveniently deployed on the surface. The observed hybrid waveguide plasmon–polariton resonances are also highly sensitive to changes in the dielectric constant[54] and could be employed for waveguide-integrated dielectric sensing applications that would additionally benefit from the field enhancement on the surface. Combining the low-loss, light-enhancing and resonant properties of plasmonic and photonic structures with NGT structures may offer new routes to hybrid devices, such as on-chip sensors, plasmonic couplers, active surface emitters, switches, and all-optical modulators.

METHODS

Numerical Simulations. All numerical simulations were performed in the frequency domain using the full-vectorial finite-element method. To calculate the spectra of the isolated trimer elements, we carried out scattering simulations with COMSOL using a two-step process: First we solved for the background field of the waveguide without the antenna using a combination of port boundary conditions (at the front and back) for waveguide mode injection, perfect electric conductor (PEC) boundary conditions (on the left and right), and perfectly matched layers (PMLs) on top and bottom. The calculation of the background field was followed by scattered-field calculations where the antenna was placed onto the waveguide. For this second step, the PEC boundaries have been replaced by PMLs, enabling outward propagation of the scattered fields in all directions to determine the scattered energy flux. For the simulation of the finite NGT, we performed single-step simulations using JCMwave. Periodic boundary conditions were used for the sides of the structure to simulate a laterally infinite tiling. PMLs were used for the continuation of the sub- and superstrate layers and the continuation of the forward and backward waveguide stack. The distance of the PMLs from the structure was chosen to be sufficiently large to avoid spurious back-reflections and to accurately resolve the out-of-plane energy flow and the in-plane transmission and reflection coefficients.

The simulations were carried out for perfectly periodic structures and for a fixed direction of excitation by injection of a TE waveguide mode along the *z*-axis. To investigate off-axis propagation and the impact of imperfections, such as spatially varying gap sizes or corner radii, one would need to conduct systematic studies on laterally and longitudinally large (and finite) structure samples, which are the subject of future work.

Conflict of Interest: The authors declare no competing financial interest.

Acknowledgment. Support by the Leverhulme Trust and the EPSRC is gratefully acknowledged.

REFERENCES AND NOTES

1. Murray, W. A.; Barnes, W. L. Plasmonic Materials. *Adv. Mater. (Weinheim, Ger.)* **2007**, *19*, 3771–3782.
2. Radko, I. P.; Volkov, V. S.; Beermann, J.; Evlyukhin, A. B.; Søndergaard, T.; Boltasseva, A.; Bozhevolnyi, S. I. Plasmonic Metasurfaces for Waveguiding and Field Enhancement. *Laser Photonics Rev.* **2009**, *3*, 575–590.
3. Schuller, J. A.; Barnard, E. S.; Cai, W.; Jun, Y. C.; White, J. S.; Brongersma, M. L. Plasmonics for Extreme Light Concentration and Manipulation. *Nat. Mater.* **2010**, *9*, 193–204.
4. Henzie, J.; Lee, J.; Lee, M. H.; Hasan, W.; Odom, T. W. Nanofabrication of Plasmonic Structures. *Annu. Rev. Phys. Chem.* **2009**, *60*, 147–165.
5. Boltasseva, A. Plasmonic Components Fabrication *via* Nanoimprint. *J. Opt. A: Pure Appl. Opt.* **2009**, *11*, 114001.
6. Stebe, K. J.; Lewandowski, E.; Ghosh, M. Oriented Assembly of Metamaterials. *Science* **2009**, *325*, 159–160.
7. Fan, J. A.; Wu, C.; Bao, K.; Bao, J.; Bardhan, R.; Halas, N. J.; Manoharan, V. N.; Nordlander, P.; Shvets, G.; Capasso, F. Self-Assembled Plasmonic Nanoparticle Clusters. *Science* **2010**, *328*, 1135–1138.
8. Duan, H.; Fernández-Domnguez, A. I.; Bosman, M.; Maier, S. A.; Yang, J. K. W. Nanoplasmonics: Classical Down to the Nanometer Scale. *Nano Lett.* **2012**, *12*, 1683–1689.
9. Tsakmakidis, K. L.; Boardman, A. D.; Hess, O. 'Trapped Rainbow' Storage of Light in Metamaterials. *Nature* **2007**, *450*, 397–401.
10. Zhang, S.; Genov, D. A.; Wang, Y.; Liu, M.; Zhang, X. Plasmon-Induced Transparency in Metamaterials. *Phys. Rev. Lett.* **2008**, *101*, 47401.
11. Liu, N.; Langguth, L.; Weiss, T.; Kästel, J.; Fleischhauer, M.; Pfau, T.; Giessen, H. Plasmonic Analogue of Electromagnetically Induced Transparency at the Drude Damping Limit. *Nat. Mater.* **2009**, *8*, 758–762.
12. Kravets, V. G.; Schedin, F.; Kabashin, A. V.; Grigorenko, A. N. Sensitivity of Collective Plasmon Modes of Gold Nanoresonators to Local Environment. *Opt. Lett.* **2010**, *35*, 956–958.
13. Zhou, W.; Odom, T. W. Tunable Subradiant Lattice Plasmons by Out-of-Plane Dipolar Interactions. *Nat. Nanotechnol.* **2011**, *6*, 423–427.
14. Maier, S. A.; Kik, P. G.; Atwater, H. A.; Meltzer, S.; Harel, E.; Koel, B. E.; Requicha, A. A. G. Local Detection of Electromagnetic Energy Transport below the Diffraction Limit in Metal Nanoparticle Plasmon Waveguides. *Nat. Mater.* **2003**, *2*, 229–232.
15. Yu, N.; Genevet, P.; Kats, M. A. M.; Aieta, F.; Tetienne, J.-P.; Capasso, F.; Gaburro, Z. Light Propagation with Phase Discontinuities: Generalized Laws of Reflection and Refraction. *Science* **2011**, *334*, 333–337.
16. Yu, N.; Aieta, F.; Genevet, P.; Kats, M. A. M.; Gaburro, Z.; Capasso, F. A Broadband, Background-Free Quarter-Wave Plate Based on Plasmonic Metasurfaces. *Nano Lett.* **2012**, *12*, 6328–6333.

17. Ni, X.; Emani, N. K.; Kildishev, A. V.; Boltasseva, A.; Shalaev, V. M. Broadband Light Bending with Plasmonic Nanoantennas. *Science* **2012**, *335*, 427.
18. Lin, J.; Mueller, J. P. B.; Wang, Q.; Yuan, G.; Antoniou, N.; Yuan, X.-C.; Capasso, F. Polarization-Controlled Tunable Directional Coupling of Surface Plasmon Polaritons. *Science* **2013**, *340*, 331–334.
19. Hess, O.; Tsakmakidis, K. L. Applied Physics. Metamaterials with Quantum Gain. *Science* **2013**, *339*, 654–655.
20. Hess, O.; Pendry, J. B.; Maier, S. A.; Oulton, R. F.; Hamm, J. M.; Tsakmakidis, K. L. Active Nanoplasmonic Metamaterials. *Nat. Mater.* **2012**, *11*, 573–584.
21. Kim, S.; Jin, J.; Kim, Y.-J.; Park, I.-Y.; Kim, Y.; Kim, S.-W. High-Harmonic Generation by Resonant Plasmon Field Enhancement. *Nature* **2008**, *453*, 757–760.
22. Tanaka, K.; Plum, E.; Ou, J. Y.; Uchino, T.; Zheludev, N. I. Multifold Enhancement of Quantum Dot Luminescence in Plasmonic Metamaterials. *Phys. Rev. Lett.* **2010**, *105*, 227403.
23. Xiao, S.; Drachev, V. P.; Kildishev, A. V.; Ni, X.; Chettiar, U. K.; Yuan, H.-K.; Shalaev, V. M. Loss-Free and Active Optical Negative-Index Metamaterials. *Nature* **2010**, *466*, 735–738.
24. Kravets, V. G.; Schedin, F.; Jalil, R.; Britnell, L.; Gorbachev, R. V.; Ansell, D.; Thackray, B.; Novoselov, K. S.; Geim, A. K.; Kabashin, A. V.; *et al*. Singular Phase Nano-Optics in Plasmonic Metamaterials for Label-Free Single-Molecule Detection. *Nat. Mater.* **2013**, *12*, 304–309.
25. Hecht, B.; Bielefeldt, H.; Novotny, L.; Inouye, Y.; Pohl, D. W. Local Excitation, Scattering, and Interference of Surface Plasmons. *Phys. Rev. Lett.* **1996**, *77*, 1889–1892.
26. Krenn, J. R.; Lamprecht, B.; Ditlbacher, H.; Schider, G.; Salerno, M.; Leitner, A.; Aussenegg, F. R. Non-Diffraction-Limited Light Transport by Gold Nanowires. *Europhys. Lett.* **2002**, *60*, 663–669.
27. Brun, M.; Drezet, A.; Mariette, H.; Chevalier, N.; Woehl, J. C.; Huant, S. Remote Optical Addressing of Single Nano-Objects. *Europhys. Lett.* **2003**, *64*, 634–640.
28. Takahara, J.; Yamagishi, S.; Taki, H.; Morimoto, A.; Kobayashi, T. Guiding of a One-Dimensional Optical Beam with Nanometer Diameter. *Opt. Lett.* **1997**, *22*, 475–477.
29. Bozhevolnyi, S. I.; Volkov, V. S.; Devaux, E.; Ebbesen, T. W. Channel Plasmon-Polariton Guiding by Subwavelength Metal Grooves. *Phys. Rev. Lett.* **2005**, *95*, 046802.
30. Oulton, R. F.; Bartal, G.; Pile, D. F. P.; Zhang, X. Confinement and Propagation Characteristics of Subwavelength Plasmonic Modes. *New J. Phys.* **2008**, *10*, 105018.
31. Holmgaard, T.; Bozhevolnyi, S. I. Theoretical Analysis of Dielectric-Loaded Surface Plasmon-Polariton Waveguides. *Phys. Rev. B* **2007**, *75*, 245405.
32. Oulton, R. F.; Sorger, V. J.; Genov, D. A.; Pile, D. F. P.; Zhang, X. A Hybrid Plasmonic Waveguide for Subwavelength Confinement and Long-Range Propagation. *Nat. Photonics* **2008**, *2*, 496–500.
33. Ditlbacher, H.; Galler, N.; Koller, D. M.; Hohenau, A.; Leitner, A.; Aussenegg, E. R.; Krenn, J. R. Coupling Dielectric Waveguide Modes to Surface Plasmon Polaritons. *Opt. Express* **2008**, *16*, 10455–10464.
34. Sorger, V. J.; Ye, Z.; Oulton, R. F.; Wang, Y.; Bartal, G.; Yin, X.; Zhang, X. Experimental Demonstration of Low-Loss Optical Waveguiding at Deep Sub-Wavelength Scales. *Nat. Commun.* **2011**, *2*, 331.
35. Sidiropoulos, T. P. H.; Maier, S. A.; Oulton, R. F. Efficient Low Dispersion Compact Plasmonic-Photonic Coupler. *Opt. Express* **2012**, *20*, 12359–12365.
36. Fort, E.; Grésillon, S. Surface Enhanced Fluorescence. *J. Phys. D: Appl. Phys.* **2008**, *41*, 013001.
37. Jain, P. K.; Xiao, Y.; Walsworth, R.; Cohen, A. E. Surface Plasmon Resonance Enhanced Magneto-Optics (SuPREMO): Faraday Rotation Enhancement in Gold-Coated Iron Oxide Nanocrystals. *Nano Lett.* **2009**, *9*, 1644–1650.
38. Johnson, P.; Christy, R. W. Optical Constants of the Noble Metals. *Phys. Rev. B* **1972**, *6*, 4370.
39. Oulton, R. F.; Sorger, V. J.; Zentgraf, T.; Ma, R.-M.; Gladden, C.; Dai, L.; Bartal, G.; Zhang, X. Plasmon Lasers at Deep Subwavelength Scale. *Nature* **2009**, *461*, 629–632.
40. Dai, D.; He, S. A Silicon-Based Hybrid Plasmonic Waveguide with a Metal Cap for a Nano-Scale Light Confinement. *Opt. Express* **2009**, *17*, 16646–16653.
41. Alam, M. Z.; Meier, J.; Aitchison, J. S.; Mojahedi, M. Propagation Characteristics of Hybrid Modes Supported by Metal-Low-High Index Waveguides and Bends. *Opt. Express* **2010**, *18*, 12971–12979.
42. Koh, A. A. L.; Fernández-Domnguez, A. I.; McComb, D. D. W.; Maier, S. A.; Yang, J. K. W. High-Resolution Mapping of Electron-Beam-Excited Plasmon Modes in Lithographically Defined Gold Nanostructures. *Nano Lett.* **2011**, *11*, 1323–1330.
43. Mühlschlegel, P.; Eisler, H.-J.; Martin, O.; Hecht, B.; Pohl, D. W. Resonant Optical Antennas. *Science* **2005**, *308*, 1607–1609.
44. Ghenuche, P.; Cherukulappurath, S.; Taminiau, T. H.; van Hulst, N. F.; Quidant, R. Spectroscopic Mode Mapping of Resonant Plasmon Nanoantennas. *Phys. Rev. Lett.* **2008**, *101*, 116805.
45. Christ, A.; Tikhodeev, S.; Gippius, N.; Kuhl, J.; Giessen, H. Waveguide-Plasmon Polaritons: Strong Coupling of Photonic and Electronic Resonances in a Metallic Photonic Crystal Slab. *Phys. Rev. Lett.* **2003**, *91*, 183901.
46. Barnes, W.; Preist, T. W.; Kitson, S. C.; Sambles, J. R. Physical Origin of Photonic Energy Gaps in the Propagation of Surface Plasmons on Gratings. *Phys. Rev. B* **1996**, *54*, 6227–6244.
47. Salomon, L.; Grillot, F.; Zayats, A. V.; de Fornel, F. Near-Field Distribution of Optical Transmission of Periodic Subwavelength Holes in a Metal Film. *Phys. Rev. Lett.* **2001**, *86*, 1110–1113.
48. Zayats, A. V.; Smolyaninov, I. I.; Maradudin, A. Nano-Optics of Surface Plasmon Polaritons. *Phys. Rep.* **2005**, *408*, 131–314.
49. Gersten, J.; Nitzan, A. Electromagnetic Theory of Enhanced Raman Scattering by Molecules Adsorbed on Rough Surfaces. *J. Chem. Phys.* **1980**, *73*, 3023.
50. Baumberg, J. J.; Kelf, T. A.; Sugawara, Y.; Cintra, S.; Abdelsalam, M. E.; Bartlett, P. N.; Russell, A. E. Angle-Resolved Surface-Enhanced Raman Scattering on Metallic Nanostructured Plasmonic Crystals. *Nano Lett.* **2005**, *5*, 2262–2267.
51. Wuestner, S.; Pusch, A.; Tsakmakidis, K. L.; Hamm, J. M.; Hess, O. Overcoming Losses with Gain in a Negative Refractive Index Metamaterial. *Phys. Rev. Lett.* **2010**, *105*, 127401.
52. Hamm, J. M.; Wuestner, S.; Tsakmakidis, K. L.; Hess, O. Theory of Light Amplification in Active Fishnet Metamaterials. *Phys. Rev. Lett.* **2011**, *107*, 167405.
53. Pusch, A.; Wuestner, S.; Hamm, J. M.; Tsakmakidis, K. L.; Hess, O. Coherent Amplification and Noise in Gain-Enhanced Nanoplasmonic Metamaterials: A Maxwell-Bloch Langevin Approach. *ACS Nano* **2012**, 2420–2431.
54. Zentgraf, T.; Zhang, S.; Oulton, R. F.; Zhang, X. Ultranarrow Coupling-Induced Transparency Bands in Hybrid Plasmonic Systems. *Phys. Rev. B* **2009**, *80*, 195415.